Journal of Materials Chemistry A

PAPER

Cite this: J. Mater. Chem. A, 2018, 6, 17192

Solution-derived glass-ceramic NaI·Na_3SbS_4 superionic conductors for all-solid-state Na-ion batteries†

Kern Ho Park,[a] Dong Hyeon Kim,[ab] Hiram Kwak,[a] Sung Hoo Jung,[ab] Hyun-Jae Lee,[b] Abhik Banerjee,[a] Jun Hee Lee[b] and Yoon Seok Jung *[a]

Received 11th June 2018
Accepted 7th August 2018

DOI: 10.1039/c8ta05537h

rsc.li/materials-a

Bulk-type all-solid-state Na-ion batteries (ASNBs) employing inorganic Na-ion conductors and operating at room temperature are considered as promising candidates for large-scale energy storage systems. However, their realization has been impeded by low ionic conductivity, instability in air of the solid electrolytes, and poor ionic contacts among the constituents of the electrodes. Here, we report novel glass-ceramic xNaI·$(1-x)Na_3SbS_4$ superionic conductors (maximum Na^+ conductivity of 0.74 mS cm^{-1} at 30 °C, for $x = 0.10$) obtained from scalable methanol solutions. Comprehensive spectroscopic evidence, density functional theory calculations, and electrochemical analysis suggest the decisive role of I^- incorporated in the disordered domains at the nanoscale in the overall Na^+ transport. Furthermore, the solution-derived NaI·Na_3SbS_4 forms uniform coating layers on the surface of the active material FeS_2, providing unobstructed ionic transport pathways in the electrodes. The good electrochemical performance of FeS_2/Na–Sn ASNBs at 30 °C is demonstrated.

1. Introduction

Large-scale energy storage systems are essential for the stable supply of electricity from renewable sources such as solar and wind power.[1,2] The cost-effectiveness of sodium-ion batteries, exploiting an earth-abundant resource, qualifies them as a highly promising alternative to the already-commercialized lithium-ion battery (LIB) technologies.[3] Furthermore, replacing conventional organic liquid electrolytes with non-flammable inorganic solid electrolytes (SEs) could extend the operating temperature of batteries up to 100 °C or higher without raising safety concerns.[4–9] For these reasons, all-solid-state Na-ion batteries (ASNBs) are considered a promising alternative.[5,7,10,11]

Sulfide SE materials are considered enablers in developing composite-structured bulk-type all-solid-state batteries.[4–8,12–14] Along with the extremely high ionic conductivities, which are comparable to those of conventional organic liquid electrolytes for several state-of-the-art materials (*e.g.*, $Li_{9.54}Si_{1.74}P_{1.44}S_{11.7}Cl_{0.3}$: 25 mS cm^{-1} at 25 °C), the softness of the sulfide materials allows two-dimensional contacts to be formed with active materials by simple mechanical pressing, avoiding the detrimental high-temperature sintering procedure.[4,5,7,8,15–17] Recently, several prototype all-solid-state lithium-ion batteries outperforming conventional LIBs were demonstrated, spurring much interest in this field.[5,6]

The exploration of sulfide Na^+ superionic conductors was initiated by the development of cubic Na_3PS_4 (0.46 mS cm^{-1} at 25 °C).[7] (Note: conductivities in this paragraph are given for 25 °C, unless otherwise stated.) The improvement in Na^+ ionic conductivity was achieved by considering solid-solutions of Na_3PS_4–Na_4SiS_4 ($94Na_3PS_4 \cdot 6Na_4SiS_4$: 0.74 mS cm^{-1}).[18] Higher conductivities were then obtained by substituting larger elements in Na_3PS_4 (Na_3PSe_4:[19] 1.16 mS cm^{-1}; Na_3SbS_4:[10,20] 1–3 mS cm^{-1}; $Na_3P_{0.62}As_{0.38}S_4$:[21] 1.46 mS cm^{-1}). In addition, new compounds of $Na_{4-x}Sn_{1-x}Sb_xS_4$ (*e.g.*, for $x = 1/3$, $Na_{11}Sn_2SbS_{12}$: 0.5 mS cm^{-1}) and $Na_{11}Sn_2PS_{12}$ (over 1 mS cm^{-1}) were identified.[22–25] Recently, Cl-doped Na_3PS_4 showing a high conductivity of 1 mS cm^{-1} was developed.[26] It is of particular importance that phosphorus-free compounds such as Na_3SbS_4 and $Na_{4-x}Sn_{1-x}Sb_xS_4$ show excellent stability in air, with no evolution of the toxic H_2S gas, in contrast to their conventional phosphorus-containing counterparts.[10,22]

To date, the majority of previous reports on superionic conductors have focused on crystalline materials, for which fast diffusion correlates with the structure,[4,6,10,19–21,23–27] but have overlooked glass or glass-ceramic SE materials. It was reported that the glass Li_4SnS_4 (0.089 mS cm^{-1} at 30 °C) exhibits higher ionic conductivity than its crystalline counterpart (0.021 mS cm^{-1} for crystalline Li_4SnS_4 at 30 °C).[8] For binary $Li_2S \cdot P_2S_5$

[a]Department of Energy Engineering, Hanyang University, Seoul, 04763, South Korea. E-mail: yoonsjung@hanyang.ac.kr

[b]School of Energy and Chemical Engineering, Ulsan National Institute of Science and Technology, Ulsan, 44919, South Korea

† Electronic supplementary information (ESI) available: X-ray powder diffraction patterns, high-resolution TEM images, X-ray photoelectron spectroscopy and Nyquist plots of NaI·Na_3SbS_4. See DOI: 10.1039/c8ta05537h

glass-ceramics, it was recently shown that the large variations in Li^+ conductivities reported in the literature originate from their glassy domains, which cannot be probed by conventional X-ray diffraction (XRD).[28–30]

Conventional preparation protocols for glass or glass-ceramic SEs include solid-state reactions at high temperature, mechanochemical methods, and melt-quenching.[5,7,31,32] Recently, wet-chemical preparation of SEs using organic solvents has emerged, and has several potential advantages such as continuous mass production and control of particle size and morphology.[5,33,34] Li_3PS_4 can be prepared using tetrahydrofuran (THF)[35] and ethyl acetate,[36] yielding moderate ionic conductivities of 0.16–0.33 mS cm^{-1}. $Li_7P_3S_{11}$ was synthesized from the solutions of dimethyl ether (DME),[37] acetonitrile (ACN),[38] and THF.[38] Significantly, the soft chemistry approach provides synthetic routes for new classes of SE materials. $Li_7P_2S_8I$ (0.63 mS cm^{-1})[39] and Li_4PS_4I (0.12 mS cm^{-1}),[40] exhibiting unprecedented crystal structures, were prepared using ACN and DME, respectively. Our group has prepared the dry-air-stable glass $0.4LiI{\cdot}0.6Li_4SnS_4$ (0.41 mS cm^{-1} at 30 °C) using homogeneous methanol (MeOH) solution.[8]

In our previous research on sulfide Na-ion SE materials, it was demonstrated that Na_3SbS_4 could be fully dissolved in protic solvents (water or MeOH) without any side reactions and then reversibly precipitated by the evaporation of the solvent.[10] However, after recovery from the solution, the Na^+ ionic conductivity had decreased by an order of magnitude (from 1.1 to 0.1 mS cm^{-1}), which could be ascribed to the lowered crystallinity or trace amounts of impurities present during the solution processes. To increase the ionic conductivity,[8,41,42] the incorporation of large and highly polarizable I^- ions was employed in this work for solution-processable Na_3SbS_4, resulting in highly conductive glass-ceramic $0.1NaI{\cdot}0.9Na_3SbS_4$ superionic conductors (0.74 mS cm^{-1} at 30 °C). The enhanced conductivity for the solution-derived $NaI{\cdot}Na_3SbS_4$ is explained by the evolution of a unique microstructure, which is investigated by a combination of spectroscopic, density functional theory (DFT), and electrochemical methods. In addition, the $0.1NaI{\cdot}0.9Na_3SbS_4$ can be deposited on the surface of the active material FeS_2 to produce a Na^+-superionically conducting layer. Compared to the FeS_2/Na–Sn ASNBs fabricated with a conventionally (*i.e.*, manually) mixed electrolyte, the battery with $0.1NaI{\cdot}0.9Na_3SbS_4$-coated FeS_2 provides a significantly enhanced electrochemical performance.

2. Experimental methods

Preparation of materials

Na_3SbS_4 powders were prepared by a solid-state reaction.[9] A stoichiometric mixture of Na_2S (Sigma Aldrich), Sb_2S_3 (99.995%, Sigma Aldrich), and elemental sulfur (99.5%, Alfa Aesar) was sealed in a fused silica ampoule under vacuum and heat-treated at 550 °C. No noticeable reaction between the product and the fused silica ampoule was found. The Na_3PS_4 powders were prepared by mechanochemical milling of a stoichiometric mixture of Na_2S and P_2S_5 (99%, Sigma Aldrich) for 10 h, followed by heat-treatment at 270 °C for 1 h in a sealed glass ampoule. For the synthesis of $NaI{\cdot}Na_3SbS_4$, the as-prepared Na_3SbS_4 powders and NaI powders (99.9%, Alfa Aesar) were fully dissolved in anhydrous MeOH (99.8%, Sigma Aldrich) and kept under dry Ar for 1 d. For a typical preparation, a solution concentration of 100 mg mL^{-1} in MeOH was used. After the solvents were removed under vacuum at room temperature, heat-treatment was carried out at different temperatures (150, 200 °C) under vacuum. Heating at higher temperatures of 300 and 550 °C was conducted in a vacuum-sealed fused silica ampoule. For the experiments in which Br was substituted for I, solution-derived $NaBr{\cdot}Na_3SbS_4$ was prepared by following the same procedure as that for $NaI{\cdot}Na_3SbS_4$. The $NaI{\cdot}Na_3SbS_4$-coated FeS_2 powders were prepared by following the same MeOH-solution process in the presence of FeS_2 (99.9%, Alfa Aesar) powders with a heat-treatment temperature of 200 °C.

Material characterization

XRD cells containing hermetically sealed SE samples with a beryllium window were mounted on a D8-Bruker Advance diffractometer equipped with Cu K_α radiation (0.154056 nm), and measured at 40 kV and 40 mA. Raman spectra were measured using a Raman spectrometer (Alpha300R, WITec) with a He–Ne laser source of wavelength 532 nm. X-ray photoelectron spectroscopy (XPS) measurements were carried out using Al K_α X-ray radiation (Sigma probe, Thermo Fisher). Field-emission scanning electron microscopy (FESEM) images were obtained using a model S-4800 instrument (Hitachi Corp.). The high-resolution transmission electron microscopy (HRTEM) image and its corresponding energy-dispersive X-ray spectroscopy (EDXS) elemental mapping images were obtained using a JEM-2100F (JEOL) operating with an acceleration voltage of 200 kV. The HRTEM image at an acceleration voltage of 80 kV was acquired using an ARM-300F (JEOL). The temperature-dependent ^{23}Na static nuclear magnetic resonance (NMR) spectra and $1/T_1$ relaxation rates were measured using a Bruker 400 MHz Avance II+ solid-state NMR at KBSI Seoul Western Center, for which the ^{23}Na resonance frequency was 105.84 MHz. NMR sample powders were sealed in a 4 mm ZrO_2 rotor in an Ar-filled glove box; all signals were obtained after a $\pi/2$ pulse. Aqueous NaCl solutions (0.1 M) were used for calibration. The Sb *K*-edge extended X-ray absorption fine structure (EXAFS) data were obtained on the BL 10C beamline (wide-energy XAFS) at the Pohang Light Source (PLS) synchrotron with a ring current of 400 mA at 2.5 GeV; the samples for EXAFS measurements were hermetically sealed by coating with a polyimide film under an Ar atmosphere.

Electrochemical characterization

The ionic conductivities of the $NaI{\cdot}Na_3SbS_4$ pellets (diameter = 6 mm) were measured by an AC impedance method, using an IviumStat analyzer (IVIUM Technologies) with Na-ion blocking Ti/SE/Ti cells. For the galvanostatic cycling tests, working electrodes were prepared from the $0.1NaI{\cdot}0.9Na_3SbS_4$-coated FeS_2 or Na_3SbS_4/FeS_2 mixture. For the mixed electrode, Na_3SbS_4 (conductivity of 1.1 mS cm^{-1} at 30 °C) prepared by solid-state synthesis at 550 °C was used. Na_3Sn alloys (nominal

composition), which exhibit a potential of ~0 V (*vs.* Na/Na^+) upon sodiation/de-sodiation, were prepared by careful mixing of Na metal (Sigma Aldrich) with Sn metal powders (99.8%, Alfa Aesar), and employed as the counter electrode. The SE layer was formed by cold-pressing 120 mg of Na_3PS_4 powders into a pellet. The as-prepared electrode material (5 mg) was spread on the top of the SE pellet, and then the as-prepared Na_3Sn was attached to the other side of the pellet, followed by pressing at 370 MPa. All the procedures were carried out in a polyaryletheretherketone (PEEK) mold (diameter = 13 mm) with two Ti metal rods as the current collectors. The cycling tests were performed at 30 °C in the range 0.6–3.0 V with a current density of 50 or 150 μA cm^{-2}.

Computational details

The first-principles calculations based on DFT were conducted using the Vienna *Ab Initio* Simulation Package (VASP) code.[43] We adopted the generalized gradient approximation method for describing the exchange–correlation generated by the Perdew–Burke–Ernzerhof functional.[44] A 4 × 4 × 4 *k*-point grid was chosen using the Monkhorst–Pack method for integrations within the Brillouin zone.[45] The energy cut-off for the plane wave basis was set at 520 eV and the force criterion for the structural optimization was 0.001 eV $Å^{-1}$. The unit cell contained two formula units of t-Na_3SbS_4, with $a = b = 7.1911(8)$ Å and $c = 7.36936(1)$ Å. Under the assumption that aliovalent doping (which replaces S^{2-} with I^-) forms $Na_{3-x}SbS_{4-x}I_x$, a Na vacancy is formed around the I^- ion to maintain charge neutrality.

3. Results and discussion

Na^+ conductivities of NaI·Na_3SbS_4

For the synthesis of xNaI·$(1-x)Na_3SbS_4$, NaI, and Na_3SbS_4 powders were dissolved in anhydrous MeOH, forming a homogeneous solution. After the solvent was evaporated under vacuum at 30 °C, the resulting powder samples were heat-treated under vacuum at temperatures of 150, 200, or 300 °C, which are high enough to remove the residual MeOH.[10]

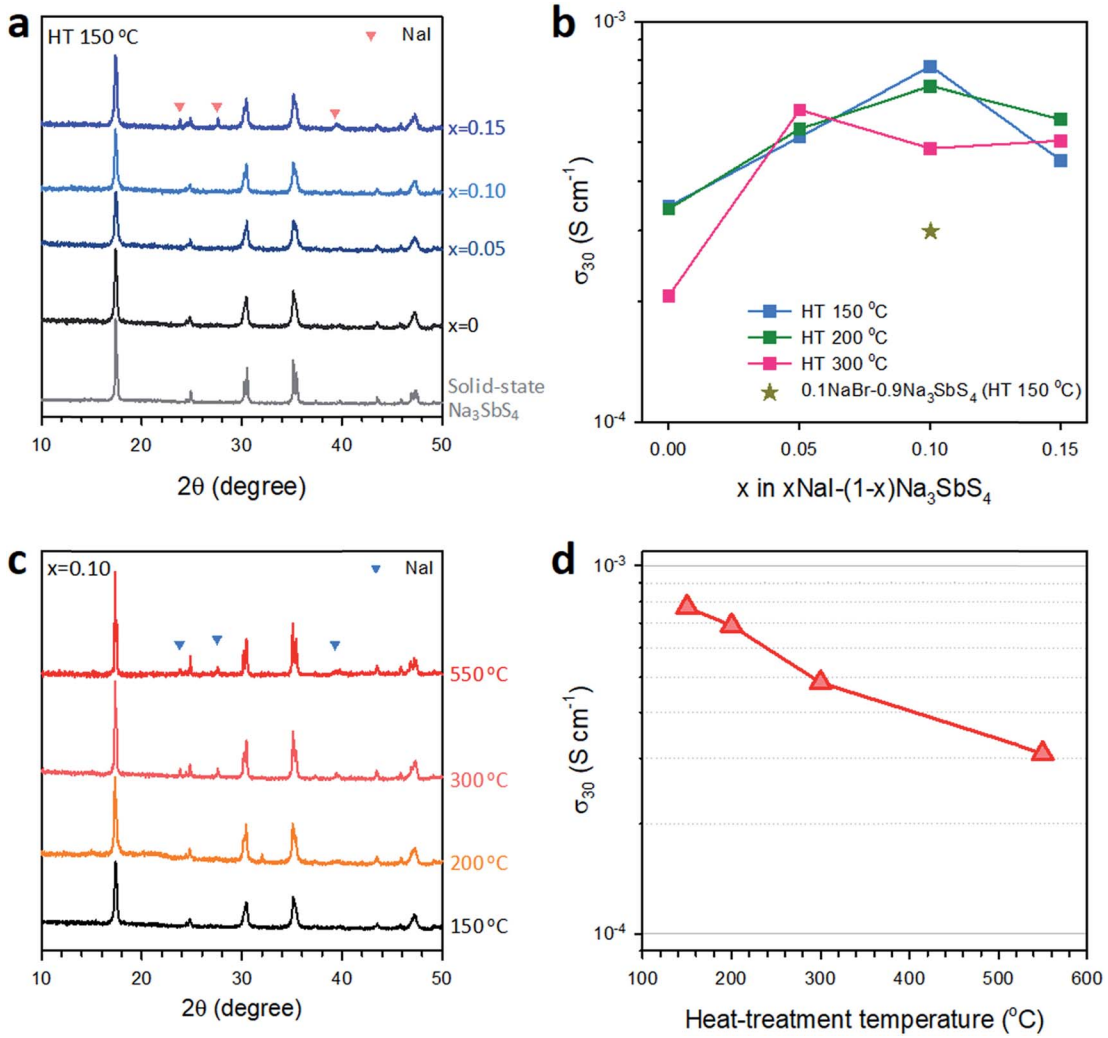

Fig. 1 XRD patterns and Na^+-ionic conductivities for solution-derived xNaI·$(1-x)Na_3SbS_4$. (a) XRD patterns of xNaI·$(1-x)Na_3SbS_4$ prepared at 150 °C. The XRD pattern for solid-state-synthesized Na_3SbS_4 is shown for comparison. (b) Na^+ ion conductivities at 30 °C for xNaI·$(1-x)Na_3SbS_4$, showing dependence on x. Samples prepared at 150, 200, or 300 °C. The result for 0.1NaBr·0.9Na_3SbS_4 prepared at 150 °C is also shown. (c) XRD patterns and (d) Na^+ ion conductivities for 0.1NaI·0.9Na_3SbS_4 prepared at different heat-treatment temperatures.

Fig. 1a shows the XRD patterns of the solution-derived xNaI·(1 − x)Na_3SbS_4 samples ($0 \leq x \leq 0.15$) prepared at 150 °C. For all the samples, the characteristic peaks of tetragonal Na_3SbS_4 are observed without any noticeable impurity peaks.[10] Compared with the pattern of the Na_3SbS_4 prepared by solid-state synthesis at 550 °C, the solution-derived xNaI·(1 − x)Na_3SbS_4 samples exhibit broader peaks, indicating lower crystallinities. Interestingly, the characteristic peaks of NaI (JCPDS no. 70-2511) were not found at $x \leq 0.10$. The Na^+ ionic conductivities of the cold-pressed SE pellets measured by the AC impedance method using Na-ion blocking Ti/SE/Ti symmetric cells are shown in Fig. 1b (typical Nyquist plots are provided in Fig. S1†). As a consequence of optimizing the synthesis protocol, the ionic conductivity of the solution-derived Na_3SbS_4 prepared at 150 or 200 °C was slightly increased to 0.34 mS cm^{-1} at 30 °C compared with our previous results (0.1–0.2 mS cm^{-1}).[10] Importantly, as NaI is added, the conductivity increases, exhibiting a maximum of 0.74 mS cm^{-1} at $x = 0.10$. This is the highest value among all inorganic SEs obtained from a homogeneous solution with low heat-treatment temperature (≤200 °C). Subsequently, when $x = 0.15$, the conductivity is lower, in line with the evolution of segregated NaI, as observed in the XRD pattern (Fig. 1a). The concurrent trends in the XRD patterns and Na^+ conductivities imply the important role of NaI and calls for a description of the mechanism for the improved ionic conductivity.

The XRD patterns (Fig. S2†) and Na^+ ionic conductivities (Fig. 1b) for xNaI·(1 − x)Na_3SbS_4 prepared at the higher temperatures of 200 and 300 °C were also compared. The samples heat-treated at 200 °C exhibit similar trends to those treated at 150 °C: maximum conductivity at $x = 0.10$ and segregation of NaI at $x = 0.15$. In contrast, for the samples treated at 300 °C, the maximum conductivity was observed for less NaI ($x = 0.05$) (Fig. 1b), and segregated NaI evolved even at $x = 0.05$ (Fig. S2b†). Fig. 1c and d show the XRD patterns and Na^+ ion conductivities for the 0.1NaI·0.9Na_3SbS_4 prepared at different heat-treatment temperatures. It is evident that as the heat-treatment temperature is increased, the segregation of NaI becomes more pronounced and the Na^+ conductivity decreases. Moreover, the drastic sharpening of the characteristic XRD peaks of Na_3SbS_4 at higher heat-treatment temperatures (Fig. 1c) implies that the evolution of crystalline NaI is associated with the increased volume fractions of the crystalline domains in the samples.

0.1NaI·0.9Na_3SbS_4 shows negligible generation of H_2S when exposed to humid air (Fig. S3†), confirming its excellent air-stability, which is in line with the other phosphorus-free Na-ion and Li-ion SE materials.[5,8,10,22,46,47] The electrochemical window for 0.1NaI·0.9Na_3SbS_4, which was obtained from the cyclic voltammetry results, is estimated to be approximately 0.5–4.5 V (*vs.* Na/Na^+) (Fig. S4†).

Microstructure and Na^+ transport for NaI·Na_3SbS_4

As the initial step to characterize the evolution of microstructures in solution-derived NaI·Na_3SbS_4, HRTEM analysis was carried out. An annular dark-field scanning TEM (ADF-STEM) image of 0.1NaI·0.9Na_3SbS_4 (prepared at 150 °C) and the corresponding elemental maps from EDXS are shown in Fig. 2a, from which a homogeneous spatial distribution of I at the nanoscale level is confirmed. The HRTEM image of the 0.1NaI·0.9Na_3SbS_4 is presented in Fig. 2b, which shows the unique glass-ceramic microstructure of nanosized crystallites surrounded by disordered domains. The corresponding fast Fourier transform (FFT) pattern (Fig. 2c) consistently shows multiple spots overlapped with diffuse ring patterns, indicating the coexistence of polycrystalline Na_3SbS_4 and amorphous phases. Another HRTEM image and its corresponding FFT pattern are also provided in Fig. S5.†

An attempt to obtain an elemental map of I at the atomic scale using higher-magnification EDXS with a low acceleration voltage of 80 kV failed due to the rapid damage of the samples by the electron beam. It is noteworthy that the crystalline Na_3SbS_4 domains do not accommodate the large I^- ions, as indicated by the evolution of segregated peaks for NaI upon crystallization of Na_3SbS_4 with increasing heat-treatment temperature (Fig. 1c). Moreover, the formation energies for the aliovalent substitution of S^{2-} in Na_3SbS_4 by I^- ($Na_{3-x}SbS_{4-x}I_x$, $x = 0.112$), obtained by DFT calculations, appear to be relatively high (~1 eV), indicating that the incorporation of I in Na_3SbS_4 is not favorable. The synthesis of I^- substituted Na_3SbS_4 ($Na_{3-x}SbS_{4-x}I_x$, $x = 0.10$) was also attempted by a solid-state reaction at 550 °C. The theoretical and experimentally obtained XRD patterns of $Na_{3-x}SbS_{4-x}I_x$ ($x = 0.112$ for the calculations; $x = 0.10$ for the experimental sample) in Fig. S6† do not match each other; specifically, the experimental XRD pattern reveals the segregation of NaI (Fig. S6a†). Moreover, the Na^+ conductivity for the sample is inferior (0.5 mS cm^{-1}) not only to that of Na_3SbS_4 (1.1 mS cm^{-1}) but also to that of the solution-derived 0.1NaI·0.9Na_3SbS_4 prepared at 150 °C (0.74 mS cm^{-1}). These results strongly suggest that the crystalline Na_3SbS_4 domains in solution-derived 0.1NaI·0.9Na_3SbS_4 could not accommodate NaI. In this context, the disordered matrix observed in Fig. 2b must be the only possible host for the accommodation of I^- ions; this interpretation is also supported by SbS_4^{3-} remaining intact under the addition of NaI, as seen in the results of the Sb *K*-edge EXAFS (Fig. 3a), Raman spectroscopy (Fig. 3b), and XPS (Fig. S7†).

To collect information about the microscopic motion of the Na^+ ions in the solution-derived NaI·Na_3SbS_4, ^{23}Na NMR analysis was carried out. The ^{23}Na static NMR spectra and $1/T_1$ relaxation rate are shown in Fig. 4 for the solution-derived Na_3SbS_4 and 0.1NaI·0.9Na_3SbS_4 prepared at 150 °C, showing the dependence on temperature. At the low temperature of 165 K, both the spectra of Na_3SbS_4 and 0.1NaI·0.9Na_3SbS_4 show asymmetric peaks, which are attributed to not only dipolar but also quadrupolar interactions of ^{23}Na.[48,49] The peaks became sharper and more symmetric at a higher temperature of 345 K, indicating that the fast Na-ionic motion averages out the interactions.[48,49] It is noteworthy that the spectra could not be fitted using a single-peak model, reflecting the coexistence of two distinct phases, possibly crystalline and glassy ones.[50] Over the entire temperature range, the spectra of the two samples are completely superimposed, which confirms the identical Na-ion

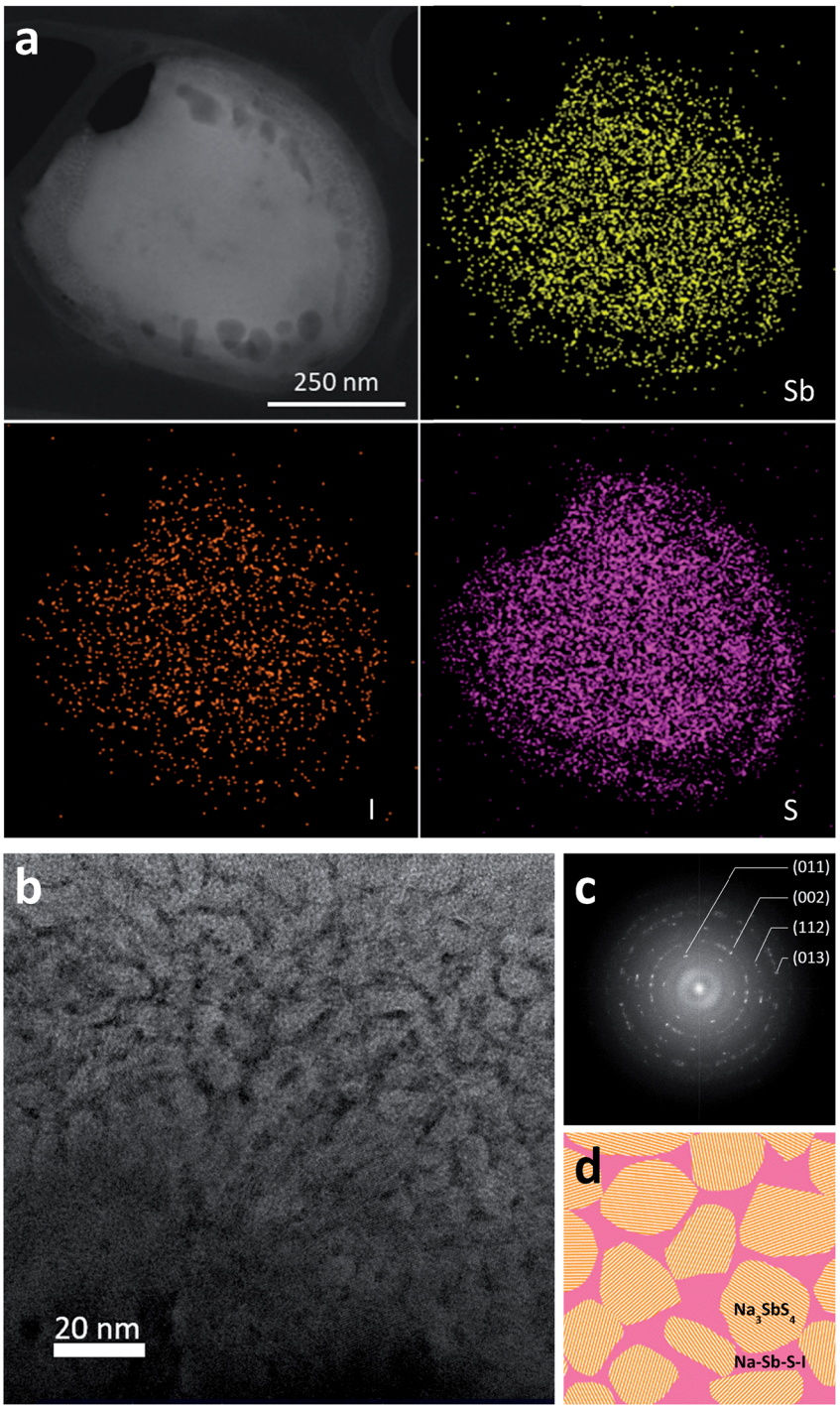

Fig. 2 TEM results for solution-derived 0.1NaI·0.9Na_3SbS_4. (a) Annular dark-field scanning TEM (ADF-STEM) image for 0.1NaI·0.9Na_3SbS_4 and its corresponding EDXS elemental maps. (b) HRTEM image of 0.1NaI·0.9Na_3SbS_4 and (c) its corresponding FFT patterns. (d) Schematic illustrating the microstructure of glass-ceramic NaI·Na_3SbS_4.

diffusion behaviors in the grains (Fig. 4a). While the spin–spin relaxation, which is used to obtain ^{23}Na static spectra such as the ones shown in Fig. 4a, is sensitive to relatively slow diffusion processes, the $1/T_1$ relaxation-rate is more sensitive to the microscopic Na^+ ion motion on a short time scale.[48] A typical $1/T_1$ plot shows three different temperature ranges: at low temperature, the Na-ion mobility is slow compared with the Larmor frequency; this range is referred to as the slow kinetic regime ($\omega_L\tau_c \ll 1$, where τ_c is the correlation time for a jump and ω_L is the Larmor frequency). In this range, $1/T_1$ exhibits an Arrhenius-type behavior. As the temperature is raised, a $1/T_1$ maximum can be achieved through the rapid motion of Na^+ ions. At this point, a jump frequency (τ_c^{-1}) has the same order of magnitude as the Larmor frequency ($\omega_L\tau_c \sim 1$).[51] Higher

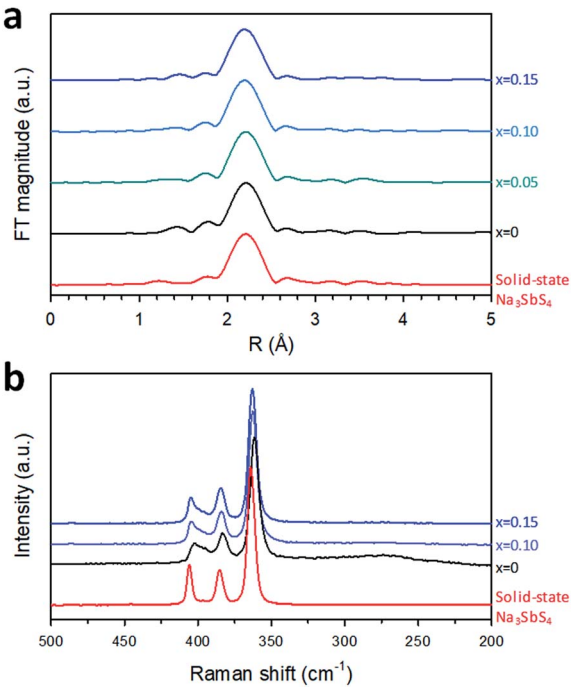

Fig. 3 Characterization of solution-derived xNaI·$(1-x)$$Na_3SbS_4$. (a) The Sb K-edge EXAFS and (b) Raman spectra of xNaI·$(1-x)$$Na_3SbS_4$ prepared at 150 °C.

temperatures than are accessible in this work would lead to a gradual decrease of $1/T_1$. In the slow kinetic regime, the NaI-added sample (0.1NaI·Na_3SbS_4) showed a slightly higher relaxation rate $1/T_1$ than the I-free sample (Fig. 4b). Importantly, the NaI-added sample reached a $1/T_1$ maximum while the I-free one remained in the slow kinetic regime, confirming the superior Na^+ ion diffusion of 0.1NaI·$0.9Na_3SbS_4$ compared to Na_3SbS_4.

The activation energies for Na^+ conductivities for the xNaI·$(1-x)$$Na_3SbS_4$ samples ($0 < x < 0.15$) prepared at different heat-treatment temperatures (150, 200, or 300 °C) are shown in Fig. S8.† For the samples heat-treated at 150 °C, the activation energy decreases as the amount of NaI is increased. In contrast, for higher heat-treatment temperatures of 200 and 300 °C, the activation energy increases when $x > 0.10$ and $x > 0.05$, respectively, which is in good accordance with the early NaI segregation (Fig. S2†). Thus, the improved conductivity might be explained by the highly polarizable I^- ions, which lower the activation barriers for ion-hopping.[8,52] Moreover, the replacement of I^- (r = 0.206 nm) by the smaller and less polarizable Br^- (r = 0.182 nm) results in lower conductivity (0.1NaBr·$0.9Na_3SbS_4$: 0.30 mS cm^{-1} (Fig. 1b)) and a higher activation energy (0.33 eV), which supports our interpretation. From these various complementary analyses, it is a reasonable conclusion that the I^- ions are selectively distributed in disordered domains at the nanoscale level and facilitate the facile movements of Na^+ ions as a result of their high polarizability, which lowers the activation barrier. Furthermore, a comprehensive study using pair distribution function analysis would be ideal to elucidate the complicated microstructural evolution in glassy phases and its relevant diffusion behavior in this glass-ceramic material.[29,30]

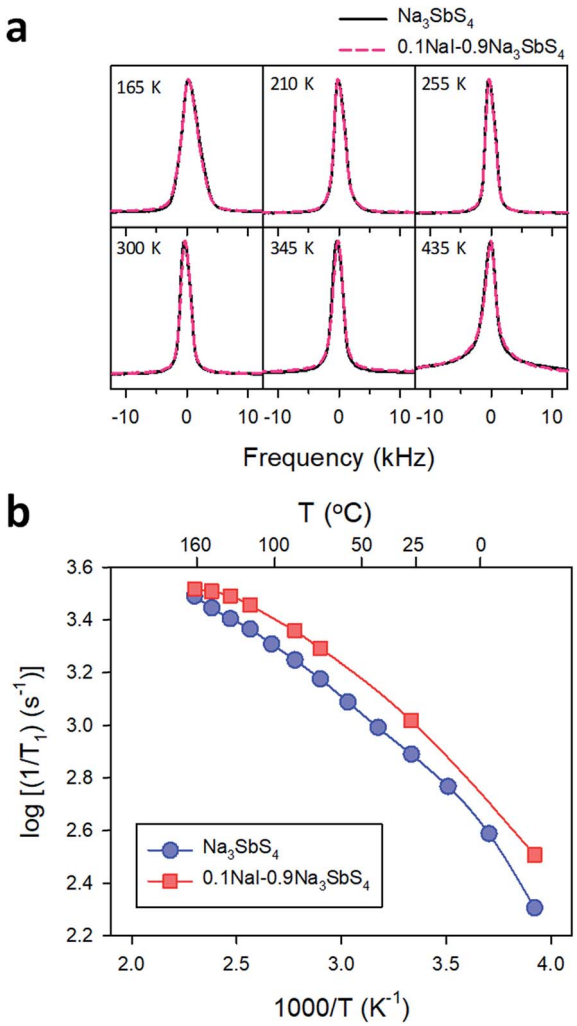

Fig. 4 Results of static solid-state ^{23}Na NMR for the solution-derived Na_3SbS_4 and 0.1NaI·$0.9Na_3SbS_4$ prepared at 150 °C. (a) ^{23}Na NMR spectra and (b) spin-lattice relaxation rate $1/T_1$, for different temperatures for Na_3SbS_4 and 0.1NaI·$0.9Na_3SbS_4$.

NaI·Na_3SbS_4-coated FeS_2

For the assessment of ASNBs, employing the solution-derived NaI·Na_3SbS_4, 0.1NaI·$0.9Na_3SbS_4$-coated FeS_2 was prepared by adding FeS_2 powder to the MeOH solution containing NaI and Na_3SbS_4. FeS_2 was chosen as the active material owing to its chemical stability to protic solvents, moderate operating voltage, good electrical conductivity, and low cost.[53] In the XRD pattern of the as-obtained product (Fig. 5a), the characteristic peaks of FeS_2 (JCPDS no. 42-1340) and Na_3SbS_4 (ref. 10) were observed without any noticeable impurities. Fig. 5b shows a field-emission scanning electron microscopy (FESEM) image of the 0.1NaI·$0.9Na_3SbS_4$-coated FeS_2 particles and its corresponding EDXS elemental maps, confirming that the SE coatings are uniformly distributed on the FeS_2.

The effects of SE-coatings on active materials were assessed by comparing the electrochemical performance of FeS_2/Na_3Sn cells fabricated with the 0.1NaI·$0.9Na_3SbS_4$-coated FeS_2 electrodes to the performance of cells prepared by the manual

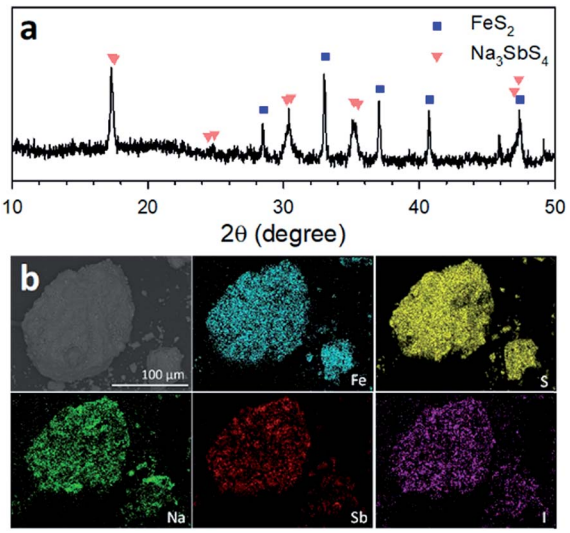

Fig. 5 Analyses of FeS_2 coated with $0.1NaI{\cdot}0.9Na_3SbS_4$ for all-solid-state Na-ion batteries (ASNBs). (a) XRD pattern and (b) FESEM image for $0.1NaI{\cdot}0.9Na_3SbS_4$-coated FeS_2 and its corresponding EDXS elemental maps.

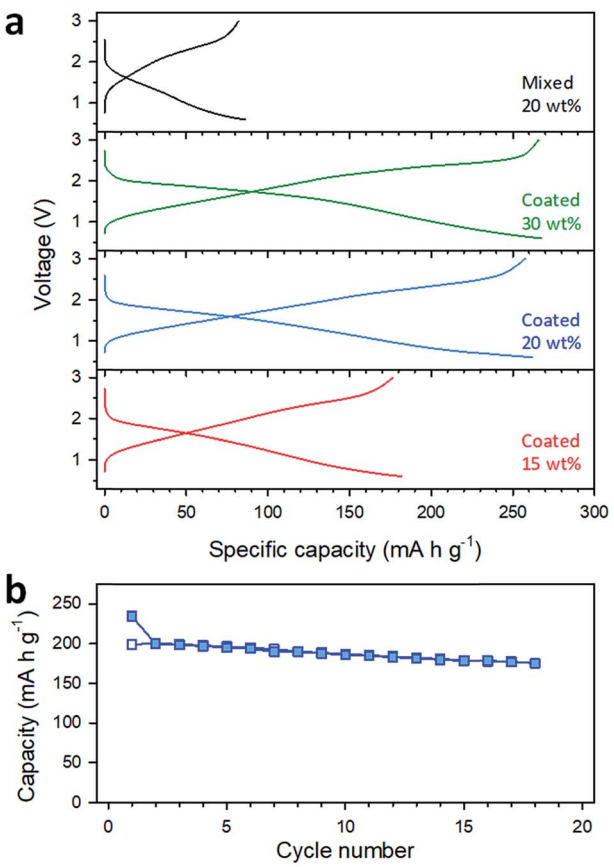

Fig. 6 (a) Second-cycle discharge–charge voltage profiles at 50 μA cm^{-2} and 30 °C for $FeS_2/Na_3PS_4/Na_3Sn$ all-solid-state cells employing the mixed and coated electrodes. (b) Cycling performance of $FeS_2/Na_3PS_4/Na_3Sn$ cell employing the $0.1NaI{\cdot}0.9Na_3SbS_4$-coated FeS_2 electrode (20 wt% coated) at 150 μA cm^{-2} and 30 °C.

mixing of FeS_2 and Na_3SbS_4. No carbon materials were added to the electrodes. Although FeS_2 could take up as many as four Na^+ ions by intercalation and the subsequent conversion reaction,[53] a voltage range of 0.6–3.0 V was adopted to avoid a large dimensional change during the conversion reaction and other detrimental side-reactions of SEs. Fig. 6a shows the discharge–charge voltage profiles for FeS_2/Na_3Sn cells at the second cycle at 50 μA cm^{-1}. The weight fraction of SEs was optimized as 20 wt% (Fig. 6a). The coated electrode showed dramatically increased reversible capacity (258 mA h g^{-1}), compared with the mixed electrode (82 mA h g^{-1}). Considering that the conductivity of the solid-state-synthesized Na_3SbS_4 in the mixed electrode is superior to that of the $0.1NaI{\cdot}0.9Na_3SbS_4$ in the coated electrode (1.1 *versus* 0.74 mS cm^{-1}), this increased capacity for the coated electrode highlights the greater significance of intimate ionic contacts (compared to ionic conductivities) for the overall performance of ASNBs.[8,10,47,54] The good cycling performance for FeS_2/Na_3Sn ASNBs employing the $0.1NaI{\cdot}0.9Na_3SbS_4$-coated FeS_2 electrode is shown in Fig. 6b. The charge–discharge voltage profiles of FeS_2/Na_3Sn cells at various current densities are shown in Fig. S9.† However, it should be noted that the rate capability of the FeS_2/Na_3Sn cells is significantly affected by Na_3PS_4 (~0.1 mS cm^{-1}) used in the separating Na_3SbS_4/Na_3PS_4 bilayer and unstable interfaces between Na_3PS_4 and Na_3Sn (Fig. S10†).[14,15,55,56]

4. Conclusion

Novel highly conductive solution-derived Na^+ superionic conductors, the glass-ceramics xNaI·(1 − x)Na_3SbS_4 (0.74 mS cm^{-1} for x = 0.1, at 30 °C), were prepared from homogeneous MeOH solutions, and applied onto the surfaces of active materials (FeS_2) to provide Na^+-superionically conductive coating layers for ASNBs. Analysis using the complementary methods of XRD, HRTEM, ^{23}Na NMR spectroscopy, Raman spectroscopy, EXAFS, XPS, DFT calculations, and electrochemical measurements indicates the selective distribution of I at the nanoscale in the disordered domains around the Na_3SbS_4 crystallites, which promotes facile Na^+ transport. These results highlight the importance of microstructures in superionic conducting materials, which cannot be produced using conventional synthesis protocols. Specifically, it is suggested that the overall ionic conductivities can be improved by engineering the grain boundary regions, an aspect which might be overlooked. Finally, a dramatic improvement in the electrochemical performance of FeS_2/Na_3Sn ASNBs using solution-derived $0.1NaI{\cdot}0.9Na_3SbS_4$ coatings on FeS_2 compared to cells prepared by conventional manual mixing was demonstrated. We believe that these results will provide new insights for the design and synthesis of Na^+ superionic conductors and contribute to the development of practical ASNBs.

Conflicts of interest

There are no conflicts to declare.

Acknowledgements

Y. S. J. research was supported by the Technology Development Program to Solve Climate Changes and by Basic Science Research Program of the National Research Foundation (NRF) funded by the Ministry of Science & ICT (grant no. NRF-2017M1A2A2044501 and 2018R1A2B6004996), by the National Research Council of Science & Technology (NST) grant by the Korea government (MSIT) (No. CAP-18-AB-1300), and by the Materials and Components Technology Development Program of MOTIE/KEIT (grant No. 10076731). J. H. L. acknowledges the support from Creative Materials Discovery Program through the NRF (2017M3D1A1040828).

References

1 J. B. Goodenough and Y. Kim, *Chem. Mater.*, 2010, **22**, 587–603.
2 B. Dunn, H. Kamath and J.-M. Tarascon, *Science*, 2011, **334**, 928–935.
3 N. Yabuuchi, K. Kubota, M. Dahbi and S. Komaba, *Chem. Rev.*, 2014, **114**, 11636–11682.
4 Y. S. Jung, D. Y. Oh, Y. J. Nam and K. H. Park, *Isr. J. Chem.*, 2015, **55**, 472–485.
5 K. H. Park, Q. Bai, D. H. Kim, D. Y. Oh, Y. Zhu, Y. Mo and Y. S. Jung, *Adv. Energy Mater.*, 2018, **8**, 1800035.
6 Y. Kato, S. Hori, T. Saito, K. Suzuki, M. Hirayama, A. Mitsui, M. Yonemura, H. Iba and R. Kanno, *Nat. Energy*, 2016, **1**, 16030.
7 A. Hayashi, K. Noi, A. Sakuda and M. Tatsumisago, *Nat. Commun.*, 2012, **3**, 856.
8 K. H. Park, D. Y. Oh, Y. E. Choi, Y. J. Nam, L. Han, J.-Y. Kim, H. Xin, F. Lin, S. M. Oh and Y. S. Jung, *Adv. Mater.*, 2016, **28**, 1874–1883.
9 X. Han, Y. Gong, K. K. Fu, X. He, G. T. Hitz, J. Dai, A. Pearse, B. Liu, H. Wang, G. Rubloff, Y. Mo, V. Thangadurai, E. D. Wachsman and L. Hu, *Nat. Mater.*, 2017, **16**, 572–579.
10 A. Banerjee, K. H. Park, J. W. Heo, Y. J. Nam, C. K. Moon, S. M. Oh, S.-T. Hong and Y. S. Jung, *Angew. Chem., Int. Ed.*, 2016, **55**, 9634–9638.
11 Y. Yan, R.-S. Kühnel, A. Remhof, L. Duchêne, E. C. Reyes, D. Rentsch, Z. Łodziana and C. Battaglia, *Adv. Energy Mater.*, 2017, **7**, 1700294.
12 T. A. Yersak, H. A. Macpherson, S. C. Kim, V.-D. Le, C. S. Kang, S.-B. Son, Y.-H. Kim, J. E. Trevey, K. H. Oh, C. Stoldt and S.-H. Lee, *Adv. Energy Mater.*, 2013, **3**, 120–127.
13 Y. J. Nam, D. Y. Oh, S. H. Jung and Y. S. Jung, *J. Power Sources*, 2018, **375**, 93–101.
14 Y. J. Nam, K. H. Park, D. Y. Oh, W. H. An and Y. S. Jung, *J. Mater. Chem. A*, 2018, **6**, 14867–14875.
15 Y. J. Nam, S. J. Jo, D. Y. Oh, J. M. Im, S. Y. Kim, J. H. Song, Y. G. Lee, S. Y. Lee and Y. S. Jung, *Nano Lett.*, 2015, **15**, 3317–3323.
16 K. H. Kim, Y. Iriyama, K. Yamamoto, S. Kumazaki, T. Asaka, K. Tanabe, C. A. J. Fisher, T. Hirayama, R. Murugan and Z. Ogumi, *J. Power Sources*, 2011, **196**, 764–767.
17 S. Ohta, J. Seki, Y. Yagi, Y. Kihira, T. Tani and T. Asaoka, *J. Power Sources*, 2014, **265**, 40–44.
18 N. Tanibata, K. Noi, A. Hayashi and M. Tatsumisago, *RSC Adv.*, 2014, **4**, 17120–17123.
19 L. Zhang, K. Yang, J. Mi, L. Lu, L. Zhao, L. Wang, Y. Li and H. Zeng, *Adv. Energy Mater.*, 2015, **5**, 1501294.
20 H. Wang, Y. Chen, Z. D. Hood, G. Sahu, A. S. Pandian, J. K. Keum, K. An and C. Liang, *Angew. Chem., Int. Ed.*, 2016, **55**, 8551–8555.
21 Z. Yu, S.-L. Shang, J.-H. Seo, D. Wang, X. Luo, Q. Huang, S. Chen, J. Lu, X. Li, Z.-K. Liu and D. Wang, *Adv. Mater.*, 2017, **29**, 1605561.
22 J. W. Heo, A. Banerjee, K. H. Park, S.-T. Hong and Y. S. Jung, *Adv. Energy Mater.*, 2017, **8**, 1702716.
23 W. D. Richards, T. Tsujimura, L. J. Miara, Y. Wang, J. C. Kim, S. P. Ong, I. Uechi, N. Suzuki and G. Ceder, *Nat. Commun.*, 2016, **7**, 8.
24 M. Duchardt, U. Ruschewitz, S. Adams, S. Dehnen and B. Roling, *Angew. Chem., Int. Ed.*, 2018, **57**, 1351–1355.
25 Z. Zhang, E. Ramos, F. Lalère, J. Assoud, K. Kaup, P. Hartman and L. F. Nazar, *Energy Environ. Sci.*, 2018, **11**, 87–93.
26 I. H. Chu, C. S. Kompella, H. Nguyen, Z. Y. Zhu, S. Hy, Z. Deng, Y. S. Meng and S. P. Ong, *Sci. Rep.*, 2016, **6**, 33733.
27 R. P. Rao, H. Chen, L. L. Wong and S. Adams, *J. Mater. Chem. A*, 2017, **5**, 3377–3388.
28 C. Dietrich, M. Sadowski, S. Sicolo, D. A. Weber, S. J. Sedlmaier, K. S. Weldert, S. Indris, K. Albe, J. Janek and W. G. Zeier, *Chem. Mater.*, 2016, **28**, 8764–8773.
29 C. Dietrich, D. A. Weber, S. J. Sedlmaier, S. Indris, S. P. Culver, D. Walter, J. Janek and W. G. Zeier, *J. Mater. Chem. A*, 2017, **5**, 18111–18119.
30 S. Shiotani, K. Ohara, H. Tsukasaki, S. Mori and R. Kanno, *Sci. Rep.*, 2017, **7**, 6972.
31 Y. Seino, T. Ota, K. Takada, A. Hayashi and M. Tatsumisago, *Energy Environ. Sci.*, 2014, **7**, 627–631.
32 K. Minami, F. Mizuno, A. Hayashi and M. Tatsumisago, *Solid State Ionics*, 2007, **178**, 837–841.
33 D. Y. Oh, D. H. Kim, S. H. Jung, J.-G. Han, N.-S. Choi and Y. S. Jung, *J. Mater. Chem. A*, 2017, **5**, 20771–20779.
34 Y. Wang, D. Lu, M. Bowden, P. Z. El Khoury, K. S. Han, Z. D. Deng, J. Xiao, J.-G. Zhang and J. Liu, *Chem. Mater.*, 2018, **30**, 990–997.
35 Z. Lin, Z. Liu, N. J. Dudney and C. Liang, *ACS Nano*, 2013, **7**, 2829–2833.
36 N. H. H. Phuc, M. Totani, K. Morikawa, H. Muto and A. Matsuda, *Solid State Ionics*, 2016, **288**, 240–243.
37 S. Ito, M. Nakakita, Y. Aihara, T. Uehara and N. Machida, *J. Power Sources*, 2014, **271**, 342–345.
38 R. C. Xu, X. H. Xia, Z. J. Yao, X. L. Wang, C. D. Gu and J. P. Tu, *Electrochim. Acta*, 2016, **219**, 235–240.
39 E. Rangasamy, Z. Liu, M. Gobet, K. Pilar, G. Sahu, W. Zhou, H. Wu, S. Greenbaum and C. Liang, *J. Am. Chem. Soc.*, 2015, **137**, 1384–1387.
40 S. J. Sedlmaier, S. Indris, C. Dietrich, M. Yavuz, C. Dräger, F. von Seggern, H. Sommer and J. Janek, *Chem. Mater.*, 2017, **29**, 1830–1835.

41 P. G. Bruce, *Solid state electrochemistry*, Cambridge University, 1995.
42 S. Ujiie, A. Hayashi and M. Tatsumisago, *Solid State Ionics*, 2012, **211**, 42–45.
43 G. Kresse and J. Furthmuller, *Comput. Mater. Sci.*, 1996, **6**, 15–50.
44 J. P. Perdew, K. Burke and M. Ernzerhof, *Phys. Rev. Lett.*, 1996, **77**, 3865–3868.
45 H. J. Monkhorst and J. D. Pack, *Phys. Rev. B*, 1976, **13**, 5188–5192.
46 T. W. Kim, K. H. Park, Y. E. Choi, J. Y. Lee and Y. S. Jung, *J. Mater. Chem. A*, 2018, **6**, 840–844.
47 Y. E. Choi, K. H. Park, D. H. Kim, D. Y. Oh, H. R. Kwak, Y.-G. Lee and Y. S. Jung, *ChemSusChem*, 2017, **10**, 2605–2611.
48 C. Yu, S. Ganapathy, N. J. J. de Klerk, E. R. H. van Eck and M. Wagemaker, *J. Mater. Chem. A*, 2016, **4**, 15095–15105.
49 K. K. Inglis, J. P. Corley, P. Florian, J. Cabana, R. D. Bayliss and F. Blanc, *Chem. Mater.*, 2016, **28**, 3850–3861.
50 M. Wilkening, D. Bork, S. Indris and P. Heitjans, *Phys. Chem. Chem. Phys.*, 2002, **4**, 3246–3251.
51 H. Paul and I. Sylvio, *J. Phys.: Condens. Matter*, 2003, **15**, R1257.
52 R. Kanno and M. Murayama, *J. Electrochem. Soc.*, 2001, **148**, A742–A746.
53 Y. Xiao, S. H. Lee and Y.-K. Sun, *Adv. Energy Mater.*, 2017, **7**, 1601329.
54 D. H. Kim, D. Y. Oh, K. H. Park, Y. E. Choi, Y. J. Nam, H. A. Lee, S.-M. Lee and Y. S. Jung, *Nano Lett.*, 2017, **17**, 3013–3020.
55 B. R. Shin, Y. J. Nam, D. Y. Oh, D. H. Kim, J. W. Kim and Y. S. Jung, *Electrochim. Acta*, 2014, **146**, 395–402.
56 S. Wenzel, T. Leichtweiss, D. A. Weber, J. Sann, W. G. Zeier and J. Janek, *ACS Appl. Mater. Interfaces*, 2016, **8**, 28216–28224.